Phantom Study of an In-House Amplitude-Gating Respiratory Method with Silicon Photomultiplier Technology Positron Emission Tomography/Computed Tomography.

Pascal Bailly, Roger Bouzerar, Romain Galan, Marc-Etienne Meyer

To cite this version:

Pascal Bailly, Roger Bouzerar, Romain Galan, Marc-Etienne Meyer. Phantom Study of an In-House Amplitude-Gating Respiratory Method with Silicon Photomultiplier Technology Positron Emission Tomography/Computed Tomography.. Computer Methods and Programs in Biomedicine, 2022, 221, pp.106907. 10.1016/j.cmpb.2022.106907 . hal-03692953

HAL Id: hal-03692953
https://u-picardie.hal.science/hal-03692953v1

Submitted on 22 Jul 2024

Version of Record: https://www.sciencedirect.com/science/article/pii/S0169260722002899
Manuscript_6ba9e4c33351a541cf7550da882fb541

Phantom study of an in-house amplitude-gating respiratory method with silicon photomultiplier technology positron emission tomography/computed tomography.

Pascal Bailly[1], Roger Bouzerar[1], Romain Galan[1,2], Marc-Etienne Meyer[1,2]

[1]Nuclear Medicine Department, Amiens University Medical Center, Amiens, France

[2]Jules Verne University of Picardie, Amiens, France

Contact details for each author:
Pascal Bailly, MSc: Department of Nuclear Medicine, Amiens University Hospital, Amiens, France. Bailly.Pascal@chu-amiens.fr
Roger Bouzerar, PhD: Department of Nuclear Medicine, Amiens University Hospital, Amiens, France. Bouzerar.Roger@chu-amiens.fr
Romain Galan: Department of Nuclear Medicine, Amiens University Hospital, Amiens, France. Galan.Romain@chu-amiens.fr
Marc-Etienne Meyer, MD, PhD: Department of Nuclear Medicine, Amiens University Hospital, Amiens, France. Meyer.Marc-Etienne@chu-amiens.fr

Address for correspondence and reprints:

Pascal Bailly

Service de Médecine Nucléaire, unité TEP

Centre Universitaire Hospitalier Amiens - Picardie

F-80054 Amiens cedex

France

Phone: +33-322-455-967; fax: +33-322-456-011

E-mail: bailly.pascal@chu-amiens.fr

ABSTRACT

Purpose: The objective of this phantom study was to determine whether breathing-synchronized, silicon photomultiplier (SiPM)-based PET/CT has a suitable acquisition time for routine clinical use.

Methods: Acquisitions were performed in list mode on a 4-ring SiPM-based PET/CT system. The experimental setup consisted of an external respiratory tracking device placed on a commercial dynamic thorax phantom containing a sphere filled with [F-18]-

fluorodeoxyglucose. Three-dimensional sinusoidal motion was imposed on the sphere. Data were processed using frequency binning and amplitude binning (the "DMI” and “OFFLINE” methods, respectively). PET sinograms were reconstructed with a Bayesian penalized likelihood algorithm.

Results: Respiratory gating from a 150-sec acquisition was successful. The DMI and OFFLINE methods gave similar activity profiles but both were slightly shifted in space; the latter profile was closest to the reference acquisition.

Conclusion: With SiPM PET/CT systems, the amplitude-based processing of breathing-synchronized data is likely to be feasible in routine clinical practice.

Key words : silicon photomultiplier; 18F-FDG PET/CT; respiratory gating; dynamic thorax phantom;

1. Introduction

The [F-18]-fluorodeoxyglucose (18F-FDG) positron emission tomography (PET) modality is a widely used for the diagnosis [1], staging [2] and follow-up [3] of lung and abdominal tumors, amongst others. These imaging assessments can only be achieved satisfactorily if the radioactive uptake' anatomical location is reliably determined and if the emission uptakes are properly quantified. These two conditions can now be met by coupling a PET system to a computed tomography (CT) system; this avoids the need to use an algorithm to co-register functional and anatomical images. The acquiring of morphological (i.e. CT modality) and functional (i.e. PET modality) data during the same examination enables the physician to precisely determine the tumor site but to correct the PET image for attenuation and scatter [4].

The organs in the chest are subject to respiratory movement. When these organs are imaged, the movement biases quantification of the uptake and may cause the uptake volume to be overestimated [5]. A range of hardware and software solutions have therefore been developed to compensate for or correct this phenomenon [6]. For example, the latest PET/CT systems can now be synchronized with the patient's breathing. Typically, the software solutions implemented on clinical consoles involve frequency-based respiratory movement compensation, although amplitude-based methods are known to be superior [7].

However, amplitude-based methods require 10 to 20 minutes of additional acquisitions when implemented on PET systems equipped with photomultiplier tubes (PMTs). This long duration is due to the fact that amplitude-based methods for respiratory movement compensation only used part of the acquired data [6]. Hence, amplitude-based methods are not easily compatible with a conventional clinical workflow.

The recent replacement of PMTs by silicon photomultipliers (SiPMs, i.e. arrays of avalanche photodiodes connected in parallel in Geiger mode) has improved the performance of PET/CT systems; the acquisition time is markedly shorter [8] and less radioactivity is injected into the patient [9]. SiPM-based PET/CT systems are much more sensitive than PMT-based systems [10,11].

The objective of the present phantom study was to compare an amplitude-based technique (implemented with in-house software) based on the CT-based method [5] with a frequency-based method (implemented with the manufacturer's software) for a 2- to 3-min breathing-synchronized acquisition (the length used in routine clinical practice) on a SiPM-based PET/CT system.

2. Materials and Methods

2.1. Acquisition systems

2.1.1. The PET/CT gantry

All the acquisitions in the present study were made in time-of-flight (TOF) mode on a 4-ring whole-body SiPM-based PET/CT system (Discovery Meaningful Insights (DMI), General Electric (GE) Healthcare, Waukesha, WI, USA), hereafter referred to as a 4-ring DMI. The PET system's axial and transaxial fields of view measured 198 and 700 mm, respectively [12]. The 4-ring DMI is equipped with 19584 lutetium-yttrium-orthosilicate (LYSO) scintillator crystals (each of which measured 5.3 mm x 3.95 mm x 25 mm) integrated into a 9 x 4 detector block. The LYSOs with a Hamamatsu SiPM array (the LightBurst digital detector) are combined with an application-specific integrated circuit (ASIC) developed in-house by GE. Thus, the output energy is digitized by an external analog-to-digital converter and the synchronization signal is digitized by an external time-digital converter. Converting the photosensor signals provides energy, position, and time information for each single event detected. The ASIC also makes it possible to record inter-block Compton scatter events [13]. The system's energy window was set to 425–650 keV. The coincidence timing window was set to 4.9 ns [14], and the TOF information was acquired and encoded with a time resolution of less than 400 full width at half-maximum (FWHM) ps [15].

The 4-ring DMI was equipped with a 64-slice CT scanner (Revolution^{TM} EVO CT, GE Healthcare, Waukesha, WI) that can generate a slice thickness from 0.63 to 10 mm and from 0.35 to 1 s in increments of 0.1 per rotation [16]. The diameter of the field of view is 700 mm.

The flowchart in Fig. 1 shows the steps described below.

2.1.2. External respiratory gating

Respiratory gating was performed using the Varian Real-time Position Management™ (RPM) device (Varian Medical Systems, Palo Alto, CA). The RPM system comprises an infrared video camera mounted on the end of the 4-ring DMI table and a reflective sensor placed on the patient's xiphoid process [17]. The system's laptop computer and dedicated software enables the user to configure and launch acquisitions, store measurements, and send synchronization triggers and data to the PET/CT acquisition console.

2.2. Data acquisition

2.2.1. Characteristics of the phantom

We performed the study with an anthropomorphic thorax phantom (Dynamic Thorax Phantom, CIRS Inc., Norfolk, VA, USA; Fig. 5 a) [18]. A 0.5 mL sphere (inner diameter: 9.89 mm; Fig. 5 c) was filled with an 18F-FDG solution and placed in the PET/CT insert of the phantom. The insert moved parallel to the table axis (corresponding to craniocaudal motion, hereafter referred to as "z displacement") but also along the x and y axes (Fig. 5 b). An up-and-down movement was therefore applied to the reflective sensor (4 of Fig. 5 a), as is done when a patient is being imaged. In clinical practice, the cube is typically placed on the patient's xiphoid process.

2.2.2. Static sphere

A reference PET/CT acquisition (REF) enabled us to measure the degree of similarity between the LM2SINO procedure and the Q.Clear module (i.e DMI Q.Clear) implemented on the 4-ring DMI console, and the Q.Clear module (i.e. OFFLINE Q.Clear), implemented on the remote PC (Fig. 1).

2.2.3. Three-dimensional motion of the sphere.

For this 150-sec acquisition, the sphere was subjected to helical movement with three sinusoidal components:

$$\begin{cases} x = 10\sin\left(\frac{\pi}{2}t\right) \\ y = 10\sin\left(\frac{\pi}{2}t\right) \\ z = 40\sin\left(\frac{\pi}{2}t\right) \end{cases} \qquad \text{(equation 1)}$$

where x, y and z correspond to the right-left, anterio-posterior and head-feet axes, respectively.

The z amplitude (i.e. 40 mm) and the respiratory cycle period (4 sec) correspond to the literature values [19].

2.3. Data features

2.3.1. PET data

During the three-dimensional acquisition, the raw emission data (i.e. prompts = trues+randoms+scatter) were stored in real time in a list-mode (LM) file consisting of 8-byte words with TOF information; the data were analyzed according to the crystal pair arrival times. The event word (EW)), i.e. the coordinates of the pair of crystals having detected the event's annihilation position) and the respiratory trigger word (sent by the RPM system) were also stored. Before reconstruction, the LM data were histogrammed (i.e. rebinned into sinogram (SINO) files. For our 4-ring DMI system's one-step acquisition, the SINO file corresponds to four-dimensional array with 1261 x 29 x 415 x 272 bin detectors. The procedure for LM to SINO conversion (LM2SINO) is as follows:

$$LM2SINO(EW):\ SINO(\theta, t, r, \phi) = SINO(\theta, t, r, \phi) + 1 \qquad \text{(equation 2)}$$

where EW is the 8-byte EW from the LM file, θ is the azimuthal angle, t is the timing bin, r is the transverse distance and ϕ is the co-polar angle (also referred to as the sinogram angle) [20].

The timing bins recorded in the 4-ring DMI SINO were 169 ps wide, which corresponds to about 2.54 cm along the line of response. Next, 29 bins were acquired along the line of response; the coincidence window width of 4.91 ns corresponding to 736 mm, covered the whole field of view.

2.3.2. CT data

All CT acquisitions were performed using low-dose parameters (0.5 s per rotation, 120 kV, and 20 mA. The acquisitions were carried out in 40 mm step-by-step cine mode, with continuous rotation of the tube and no current modulation. Each rotation generated 16 slices (thickness: 2.5 mm). The acquisition duration per step was based on the period of the patient's respiratory cycle.

2.3.3. Respiratory data

The amplitude of the sensor's displacement was measured every 40 msec and stored in an ASCII text file (RPM_Curve) on the RPM device. A trigger generated by the RPM was sent to the gantry as the curve started to rise after expiration.

The RPM_Curve file contains a header describing (among other things) the duration of the respiratory signal, the number of measurements performed per second, and the format of the data following the header. The data layout includes the amplitude of the reflector displacement and a binary value of the transistor-transistor logic trigger output to the 4-ring DMI.

2.4. Data processing

2.4.1. CT slice reconstruction

The CT images were reconstructed with Adaptive Statistical Iterative Reconstruction software (ASIR-V^{TM}, GE Healthcare, Waukesha, WI, USA) [21]. This hybrid iterative algorithm used for the initialization an image obtained by filtered back projection reconstruction up to 40% [22].

2.4.2. Gated CT volume construction

The respiratory gating system makes it possible to acquire and process CT and PET data according to the respiratory state. The volumes corresponding to these respiratory states (obtained by frequency or amplitude analysis) are henceforth referred to as GATEs. By convention with our 4-ring DMI, CT GATEs were generated for different target positions and expressed as a percentage (Fig. 2). Thus, $GATE_{CT}^{50\%}$ and $GATE_{CT}^{0\%}$ denote the CT volumes obtained in a time interval around the expiratory peak and the inspiration peak, respectively. Fig. 2 shows the CT gate construction process. As mentioned above, a first X-ray emission phase with 40 mm portions provides CT sinograms for the creation of CT slices. After synchronization of the respiratory signal obtained during this CT acquisition by the RPM device, the slices are binned according to their positions in space (i.e. the bed step position) and in time (i.e. the frequency position in the respiratory cycle). The retrospective construction of these GATEs can lead to interpolations on the choice of slice.

2.4.3. Frequency-based LM binning: the DMI method

In the DMI frequency-based approach implemented by the manufacturer on the acquisition console, each respiratory cycle (delimited by two RPM trigger words in the LM file) is divided into several bins [6]. In the present study, we focused on the tissue position in a window around the expiration peak (Fig. 3 b). The newly generated LM file then contains only the events corresponding to the frequency selection for the "50%" target (henceforth referred to as $GATE_{DMI}^{50\%}$).

2.4.4. Amplitude-based LM binning: the in-house OFFLINE method

In this approach, the respiratory cycle is divided into several bins as a function of its magnitude [6]. The acquisition window was placed around the expiratory peak (Fig. 3 a, henceforth referred to as $GATE_{OFFLINE}^{50\%}$). We coded the amplitude-based method in C and MATLAB (2019b, The MathWorks Inc., Natick, MA, USA) on a remote PC. Figure 4 shows the graphical interface that allows the user to set the amplitude range limits (ESR_min and ESR_max) and then generate a new LM file containing only the prompts collected during this breathing amplitude window.

There were two amplitude processing steps. Firstly, we synchronized the RPM_curve and LM files on the first synchronization trigger (denoted hereafter as T0). Secondly, we selected the events detected when the tissue was located between the amplitude range limits on the respiratory curve (Fig. 4).

2.4.5. PET volume reconstructions

The procedure for converting the LM file into a sinogram (i.e. LM2SINO, described in paragraph 2.3.1) was applied on the console (for the DMI method) or the remote PC (for the OFFLINE method). Using the SINOs obtained by the DMI and OFFLINE methods and a block sequential regularized expectation maximization penalized-likelihood reconstruction algorithm (Q.Clear™, GE Healthcare, Waukesha, WI, USA) [23], we generated the PET GATES as follows:

$$\lambda_j^{n+1} = \frac{\lambda_j^n}{A\sum_{i=1}^{nbdet} M_{i,j}} \sum_{i=1}^{nbdet} M_{i,j} \frac{Sino_i}{\sum_{j=1}^{nbvox}\left(M_{i,j}\lambda_j^n\right)} - \beta \sum_{j=1}^{nbvox} \sum_{k \in N_j} \phi\left(\lambda_j^n, \lambda_k^n\right) \qquad \text{(equation 3)}$$

The regularization function for Q.Clear was defined as follows:

$$\phi\left(\lambda_j^n, \lambda_k^n\right) = \omega_{j,k} \frac{\left(\lambda_j - \lambda_k\right)^2}{\left(\lambda_j + \lambda_k\right) + \gamma\left|\lambda_j + \lambda_k\right|} \qquad \text{(equation 4)}$$

where λ_j^n is the j^{th} voxel in iteration n, A corresponds to the attenuation correction factors, M is the system matrix, $nbdet$ is the number of detectors, $Sino_i$ is the i^{th} detector element in the sinogram, $nbvox$ is the number of voxels, β controls the weight of the prior, N_j is the set of neighbors of voxel j, ω is the weighting by the Euclidean distance (i.e. typical values of $1, {}^{1}/_{\sqrt{2}}$ and ${}^{1}/_{\sqrt{3}}$) and γ is a parameter that controls the degree of edge preservation [24].

In the present study, β was set to 550 and γ was set permanently to 2 by the manufacturer. The two PET reconstructions (i.e. DMI and OFFLINE) generated volumes of 256 x 256 x 71 voxels (pixel size: 2.73 x 2.73 mm^2; slice thickness: 2.79 mm). The effects of non-invariance in translation are also taken into account with Q.Clear reconstruction, using a point spread function modelling [25]. The TOF information [26], optional for this reconstruction, was considered for all the results described here. Moreover, corrections for singles-based estimation of random conincidences [27], CT-based scatter [28], attenuation and dead-time were applied.

We used the notation used for CT to name the PET gates, namely the $GATE_{DMI}^{50\%}$ volume generated by the DMI method and the $GATE_{OFFLINE}^{50\%}$ generated by the OFFLINE method for a respiratory position window around the expiration.

DMI reconstructions were performed with a computer containing four AMD FirePro S9150 graphics cards (4GPU – 4 x 2.5 TeraFLOPS) and OFFLINE reconstructions were performed with a computer containing an Intel® Core™ I7-7820HQ 2.9 GHz processor (CPU – 34.12 GigaFLOPS).

2.5. Data analysis

For each volume obtained, we determined the peak value (i.e. DMI_REF, OFFLINE_REF, $GATE_{DMI}^{50\%}$ and $GATE_{OFFLINE}^{50\%}$) and its voxel coordinates. The Euclidean distances between the peak value for the DMI_REF volume and the other volumes' respective peak values were calculated as follows:

$$dist(vol) = \sqrt{(x_{DMI\_REF} - x_{\max\_vol})^2 + (y_{DMI\_REF} - y_{\max\_vol})^2 + (z_{DMI\_REF} - z_{\max\_vol})^2}$$

(equation 5)

where vol ∈ { OFFLINE_REF, $GATE_{DMI}^{50\%}$, $GATE_{OFFLINE}^{50\%}$}.

The normalized mean square error (NMSE) [29] in the z axis (the Z Profile) was calculated for the difference between the DMI and OFFLINE methods, as follows:

$$NMSE_{vol} = \frac{\sum_{j=1}^{71}(Z\ Profile_j^{DMI\_REF} - Z\ Profile_j^{vol})^2}{\sum_{j=1}^{71}(Z\ Profile_j^{DMI\_REF})^2} \qquad \text{(equation 6)}$$

where *vol* ∈ {OFFLINE_REF, $GATE_{DMI}^{50\%}$, $GATE_{OFFLINE}^{50\%}$ } and *j* is the slice number.

We also calculated the full width at half-maximum (FWHM, in mm) of Z Profile passing through the maximum. The FWHM was calculated by linear interpolation between the pixels situated on either side of the peak's half-maximum in each profile. The full width at tenth-maximum (FWTM) was measured in the same way.

3. Results

The 0.5 mL sphere was filled with an 18F-FDG solution (concentration: 67.28 kBq/mL). The activity profiles of the two reconstructions (DMI_REF and OFFLINE_REF) for the static sphere (acquisition time: 120 sec) are shown in Fig. 6. The concentration was 51.61 kBq/mL at the start of the acquisition.

These Z Profiles passed through each of the two maxima: the peak values were 58.89 kBq/mL for DMI and 58.86 kBq/mL for OFFLINE. The FWHM was 7.07 mm for DMI and 7.14 mm for OFFLINE (Table 1), and the FWTM was 12.27 mm for DMI and 12.79 mm for OFFLINE (Table 1).

For the 150-sec acquisition of the moving ball, the radioactive concentration present in the sphere was 43.8 kBq/mL. Fig. 6 also shows the DMI and OFFLINE methods' respective activity profiles for acquisition of the sphere during 3D sinusoidal motion and for a gate corresponding to a window around the expiratory peak (i.e. 50%). These Z Profiles passing through each of the two maxima in $GATE_{DMI}^{50\%}$ and $GATE_{OFFLINE}^{50\%}$ were 53.89 kBq/mL for DMI and 55.65 kBq/mL for OFFLINE. The FWHM was 7.64 mm for DMI and 7.3 mm for OFFLINE, and the FWTM was 15.4 mm for DMI and 11.8 mm for OFFLINE (Table 1).

The Euclidean distances and NMSEs are also given in Table 1.

Fig. 7 (b) shows a zoomed portion of the CT coronal slice (a) for the immobile sphere (i.e. REF). The coronal image corresponding to the plane passing through the middle of the sphere for $GATE_{CT}^{50\%}$ is shown in Fig. 7 c. Figs. 7 d-g shows the sphere-centered portions of the coronal slices for the DMI_REF, OFFLINE_REF, $GATE_{DMI}^{50\%}$ and $GATE_{OFFLINE}^{50\%}$ volumes, respectively.

The time elapsed between the start of the acquisition of the moving sphere and the first synchronization trigger was 12 sec (T0). During a period of 42.51 seconds, the tissue positions ranged from 1.35 cm (ESR_min) to 1.6 cm (ESR_max), which corresponded to the expiration position. The tissues were therefore outside this window for 95.49 sec of the acquisition time.

4. Discussion

18F-FDG PET/CT is now an important tool for detecting tumors, planning radiotherapy, and evaluating treatment responses. Respiratory motion during a PET/CT acquisition can worsen image quality and can lead to errors in uptake quantification. Various frequency- and amplitude-based methods for compensating for respiratory movement have been developed. Although the amplitude-based approach has proven advantages [5,30], it has not yet been implemented on the manufacturers' consoles. In fact, amplitude-based methods have an enormous disadvantage; they are time-consuming (especially in terms of the acquisition) and thus cannot easily be included in routine clinical work flows.

The SiPM’s sensitivity greatly reduces the acquisition time. The objective of the present study was therefore to analyze amplitude-based respiratory gating with a SiPM PET camera, using in-house software.

Wagatsuma *et al.* [12] showed that the LYSO-SiPM coupling in a 4-ring DMI was 68% more sensitive than a conventional LYSO-PMT (D710; GE Healthcare, Waukesha, WI, USA); by using the NEMA NU 2-2012 standard operating procedure for a source placed in the center of the field of view, the value was 12.62 cps/kBq for the DMI and 7.50 cps/kBq for the D710. Hsu *et al.*'s study gave similar values with the 4-ring DMI at two different sites: 14.0 cps/kBq and 13.4 cps/kBq [10]. The values obtained by Economou Lundeberg *et al.*, were 6.9 cps/kBq for the PMT-based Discovery 690 (D690, GE Healthcare, Waukesha, WI, USA) and 14 cps/kBq for the 4-ring DMI [9]. The latter research group also evaluated the clinical utility of SiPM PET technology with regard to the image quality and the standard uptake value, relative to older generations of PET cameras. On the same lines, Oddstig *et al.* emphasized the value of SiPM-based systems for improving diagnostic performance [31]. The greater sensitivity of SiPM-based PET is due to several factors, such as the parallel processing of detected events via a mesh of avalanche microcells, the suppression of Anger's electronic localization, and a higher energy resolution [32].

Cui et al. [18] also used the CIRS dynamic thorax phantom to study their 4D PET/CT protocol, using a large sphere (internal diameter: 25 mm) and displacement amplitudes of 15.4 and 30.6 mm. We chose to use a sphere with a diameter of ~10 mm in the present study; this situation is more challenging because this diameter corresponded to our system's limit of detection (i.e. two or three times the spatial resolution of ~5 mm) [14]. Hence, the amplitude of the sphere's sinusoidal movement along the z axis (i.e. a simulated craniocaudal movement) was four times the sphere's diameter (i.e. 40 mm), ensuring that none of the voxels could contain activity at any time during the acquisition.

Using the same algorithm (described in the "Data Analysis" paragraph) as us, Fin et al. obtained a FWHM of 9.2 mm for an identical, static sphere [29]. This greater width (relative to our value of 7.14 mm) might be related to Fin et al.'s use of a PMT-based PET/CT system.

Reconstruction in emission tomography corresponds to a poorly posed inverse problem. Although several solutions have been developed, the Bayesian approach is used by all the manufacturers [33]. In order to eliminate the high frequencies related to noise and edges, the number of iterations and the post filter parameters must be defined. The post-filtering increases the partial volume effect, which therefore spreads the activity but also decreases the activity values. A number of older mathematical methods for regularization have been incorporated into reconstruction tools, including the Q.Clear algorithm. This algorithm is based on an accelerated block-iterative version of expectation maximization maximum likelihood algorithm (equation 3); this local, non-linear regularization method (equation 4) conserves the edges (i.e. $\gamma\left|\lambda_j + \lambda_k\right|$) and requires only one weighting parameter β.

By acquiring data for the immobile sphere, we were able to check and validate the LM2SINO process and the Q.Clear algorithm coded for the OFFLINE version. In fact, the precision of these calculations is closely linked to the development of parallelized code and the processor's architecture (whether a graphics processing unit or a central processing unit). With O(n) complexity algorithms like Q.Clear, quantization effects can occur. Given the measured value of $NMSE_{OFFLINE\_REF}$ (0.01), we can nevertheless be reasonably confident that this is not the case here. A difference in calculation precision between the DMI and OFFLINE approaches was observed for the locations of the two maxima. This difference was present not in the axial position (i.e. slice 28 for the volumes DMI_REF and OFFLINE_REF) but was present for the x and y coordinates of the transverse slices (Table 1). This partial volume effect results from a rounding-up of the position of the activities between the two volumes; the Euclidean distance evaluated here was 6.11 mm (Table 1). The distance's largest component corresponds to a difference of two 2.73 mm voxels on the x axis (i.e. 5.47 mm). This value is very close to the camera's spatial resolution of ~5 mm. (14). Furthermore, the shape of the Z Profiles confirmed that the DMI_REF and OFFLINE_REF methods (Fig. 6) were both suitable for reconstructing the activity.

The transfer of a circular dotted region of interest (ROI) (Fig. 7 b, corresponding to the edge of the sphere) to a coronal image of the $GATE_{CT}^{50\%}$ volume (Fig. 7 c) shows how difficult it was for the system to constitute the volume of a small sphere moving with an amplitude of four times its size. As shown in the block diagram in Fig. 2, the precision of the volume's definition is highly dependent on the placement of the 40 mm CT acquisition steps (which depend on the lesion to be observed) and the number and thickness of the slices generated. The latter parameters have a major influence on the increase in the patient's exposure. In turn, the CT GATE's outputs will influence the uptake's location and the precision of the attenuation correction.

It should also be noted that the position of the rod that supports the sphere is not the same in Fig. 7 c as in Fig. 7 b. This might suggest that the time synchronization between the RPM_curve file and the creation of the CT slices is imprecise.

The amplitude boundaries (ESR_min and ESR_max) are determined by the construction of these CT volumes. It is noteworthy that the value of ESR_min detected by the system (Fig. 4) is lower than the minimum position of the respiratory curve. This might constitute a limitation, since our OFFLINE method is based not only on the attenuation correction by this volume but also by the selection of the events by the bounds. Unfortunately, it is not possible for the RPM system to directly trigger X-ray emission by the 4-ring DMI; such an option would probably increase the precision of respiratory amplitude measurements.

The Z Profile for $GATE_{OFFLINE}^{50\%}$ (Fig. 6) was better located (relative to the profiles obtained for the reference acquisition with a static sphere) than the Z Profile for $GATE_{DMI}^{50\%}$. This was also true in two dimensions on the coronal image (Fig. 7 g), as shown by the red dotted circular ROI. It should be borne in mind that the table was in the same position for the reference acquisition and the acquisition of the moving sphere.

In view of the results obtained for OFFLINE with remote processing, we now intend to exploit the 4-ring DMI's computing capacity by directly loading the LM file generated by our application onto the DMI system; this will enable us to carry out a study in a clinical context.

5. Conclusion

Although the amplitude-based respiratory motion compensation method had shown its superiority over the frequency method, it had not been extensively exploited on PMT-based PET systems – partly because of the longer acquisition time required by this method. The greater sensitivity of the new SiPM-based PET systems might enable amplitude-based respiratory motion compensation algorithms to be applied more widely in a clinical context, where a short acquisition time is a key criterion.

Acknowledgments

The authors thank Michael Spohn and Chuck Stearns (GE Healthcare, Waukesha, WI) for their assistance in interpreting the list mode data files and performing offline reconstructions. We also thank Dr David Fraser (Biotech Communication SARL, Ploudalmézeau, France) for copy-editing assistance.

Figure legends

Fig. 1. Study flowchart.

Fig. 2. The manufacturer's retrospective method for generating the CT gates. Firstly, slices are reconstructed in 40 mm steps. Secondly, the images are sorted by their positions in space (i.e. the slice's position relative to the table's position) and time (i.e. according to the data in the RPM_Curve file), which makes it possible to build spatiotemporal volumes (i.e. GATE). Here, we show an example of gate binning around the expiratory (50%) and inspiratory (0%) positions.

Fig. 3. Event selection for the two methods. For the DMI (frequency-based) method in part (a), the windows around the expiratory peak are indicated on the RPM_Curve data by yellow lines. The acquisition times of the emissions detected and kept by this method are indicated by the yellow portions on the LM file shown below. Likewise, part (b) show the amplitude-based OFFLINE method. The duration of the RPM_Curve file and the portions of the LM file that are kept are indicated by green lines. The ESR_min and ESR_max boundaries are shown for comparative purposes.

Fig. 4. The interface of our OFFLINE software, which enables the user to import and visualize the respiratory curve obtained (1) with RPM during the acquisition and the LM file acquired (2). The user of manually enters the event selection range: ESR_min (3) and ESR_max (4) (red lines).

Fig. 5. The Dynamic Thorax Motion Phantom system from CIRS Inc. (a) comprises (1) a power and control unit, (2) the displacement motors, (3) the thorax phantom, and (4) a reflective sensor. (b) shows thorax phantom and the moving insert (part 5); the insert's components (including the sphere) are detailed in (c). Lastly, (d) corresponds to the maximum intensity projection of a CT acquisition of the phantom, showing the sphere within the phantom's rib cage. The z (craniocaudal) axis and the direction (from the back of the camera to the front) are shown on (a), (b), (c), and (d).

Fig. 6. Plots of activity profiles along the z axis for slices 16 to 36. The profiles pass through the maximum volumes obtained for the immobile sphere, with the manufacturer's Q.Clear method (DMI_REF) and the in-house OFFLINE method (OFFLINE_REF). Plots of the profiles for the expiration volumes (50%) and the sphere moving sinusoidally, generated by the manufacturer's frequency-based method ($GATE_{DMI}^{50\%}$) and the amplitude-based method ($GATE_{OFFLINE}^{50\%}$).

Fig. 7. The coronal sections passing through the center of the sphere (for CT volumes) or through activity peak values (for PET volumes). Part (a) shows the coronal CT slice from the REF acquisition step. Part (b) is an enlarged part of (a). Part (c) show the same portion of a coronal image for the $GATE_{CT}^{50\%}$ volume. Parts (d) to (g) show the sphere-centered portions of the coronal slices for the DMI_REF, OFFLINE_REF, $GATE_{DMI}^{50\%}$ and $GATE_{OFFLINE}^{50\%}$ volumes, respectively**.** The red dotted ROI corresponds to the edge of the sphere at the reference position (obtained from the CT image in part (b)).

REFERENCES

[1] F. Kang, W. Mu, J. Gong, S. Wang, G. Li, G. Li, W. Qin, J. Tian, J. Wang, Integrating manual diagnosis into radiomics for reducing the false positive rate of (18)F-FDG PET/CT diagnosis in patients with suspected lung cancer, Eur J Nucl Med Mol Imaging. 46 (2019) 2770–2779. https://doi.org/10.1007/s00259-019-04418-0.

[2] J.H. Yoon, J.M. Lee, W. Chang, H.-J. Kang, A. Bandos, H.-J. Lim, S.Y. Kang, K.W. Kang, S.-B. Ryoo, S.-Y. Jeong, K.J. Park, Initial M Staging of Rectal Cancer: FDG PET/MRI with a Hepatocyte-specific Contrast Agent versus Contrast-enhanced CT, Radiology. 294 (2020) 310–319. https://doi.org/10.1148/radiol.2019190794.

[3] K. Skougaard, O. Ostrup, K. Guldbrandsen, B. Sorensen, P. Meldgaard, Z. Saghir, P. Gortz, M.N. Lonsdale, M.S. Frank, O. Gerke, B.A. Rychwicka-Kielek, G. Persson, L.H. Land, T. Schytte, U. Bodtger, H. Skuladottir, J. Sogaard, S.S. Nielsen, T.R. Rasmussen, B.M. Fischer, Surveillance With PET/CT and Liquid Biopsies of Stage I-III Lung Cancer Patients After Completion of Definitive Therapy: A Randomized Controlled Trial (SUPER), Clin Lung Cancer. 21 (2020) e61–e64. https://doi.org/10.1016/j.cllc.2019.11.002.

[4] T. Beyer, D.W. Townsend, T. Brun, P.E. Kinahan, M. Charron, R. Roddy, J. Jerin, J. Young, L. Byars, R. Nutt, A combined PET/CT scanner for clinical oncology, J Nucl Med. 41 (2000) 1369–79.

[5] J. Daouk, L. Fin, P. Bailly, M.E. Meyer, Improved attenuation correction via appropriate selection of respiratory-correlated PET data, Comput Methods Programs Biomed. 92 (2008) 90–8. https://doi.org/10.1016/j.cmpb.2008.06.014.

[6] A. Pepin, J. Daouk, P. Bailly, S. Hapdey, M.E. Meyer, Management of respiratory motion in PET/computed tomography: the state of the art, Nucl Med Commun. 35 (2014) 113–22. https://doi.org/10.1097/MNM.0000000000000048.

[7] Y. Tsutsui, D. Kidera, T. Taniguchi, G. Akamatsu, I. Komiya, Y. Umezu, Y. Kitamura, S. Baba, M. Sasaki, Accuracy of amplitude-based respiratory gating for PET/CT in irregular respirations, Ann Nucl Med. 28 (2014) 770–9. https://doi.org/10.1007/s12149-014-0870-5.

[8] I. Sonni, L. Baratto, S. Park, N. Hatami, S. Srinivas, G. Davidzon, S.S. Gambhir, A. Iagaru, Initial experience with a SiPM-based PET/CT scanner: influence of acquisition time on image quality, EJNMMI Phys. 5 (2018) 9. https://doi.org/10.1186/s40658-018-0207-x.

[9] J. Economou Lundeberg, J. Oddstig, U. Bitzen, E. Tragardh, Comparison between silicon photomultiplier-based and conventional PET/CT in patients with suspected lung cancer-a pilot study, EJNMMI Res. 9 (2019) 35. https://doi.org/10.1186/s13550-019-0504-y.

[10] D.F.C. Hsu, E. Ilan, W.T. Peterson, J. Uribe, M. Lubberink, C.S. Levin, Studies of a Next-Generation Silicon-Photomultiplier-Based Time-of-Flight PET/CT System, J Nucl Med. 58 (2017) 1511–1518. https://doi.org/10.2967/jnumed.117.189514.

[11] J. Zhang, P. Maniawski, M.V. Knopp, Performance evaluation of the next generation solid-state digital photon counting PET/CT system, EJNMMI Res. 8 (2018) 97. https://doi.org/10.1186/s13550-018-0448-7.

[12] K. Wagatsuma, K. Miwa, M. Sakata, K. Oda, H. Ono, M. Kameyama, J. Toyohara, K. Ishii, Comparison between new-generation SiPM-based and conventional PMT-based TOF-PET/CT, Phys Med. 42 (2017) 203–210. https://doi.org/10.1016/j.ejmp.2017.09.124.

[13] A.A. Wagadarikar, A. Ivan, S. Dolinsky, D.L. McDaniel, Sensitivity Improvement of Time-of-Flight (ToF) PET Detector Through Recovery of Compton Scattered Annihilation Photons, IEEE Transactions on Nuclear Science. 61 (2014) 121–125. https://doi.org/10.1109/TNS.2013.2282119.

[14] A. Chicheportiche, R. Marciano, M. Orevi, Comparison of NEMA characterizations for Discovery MI and Discovery MI-DR TOF PET/CT systems at different sites and with other commercial PET/CT systems, EJNMMI Phys. 7 (2020) 4. https://doi.org/10.1186/s40658-020-0271-x.

[15] C.S. Levin, S.H. Maramraju, M.M. Khalighi, T.W. Deller, G. Delso, F. Jansen, Design Features and Mutual Compatibility Studies of the Time-of-Flight PET

Capable GE SIGNA PET/MR System, IEEE Trans Med Imaging. 35 (2016) 1907–14. https://doi.org/10.1109/TMI.2016.2537811.

[16] R. Raju, R.C. Cury, B. Precious, P. Blanke, C. Naoum, C. Arepalli, J.C. Batlle, D. Murphy, C. Hague, J.A. Leipsic, Comparison of image quality, and diagnostic interpretability of a new volumetric high temporal resolution scanner versus 64-slice MDCT, Clin Imaging. 40 (2016) 205–11. https://doi.org/10.1016/j.clinimag.2015.10.009.

[17] S.A. Nehmeh, Y.E. Erdi, T. Pan, E. Yorke, G.S. Mageras, K.E. Rosenzweig, H. Schoder, H. Mostafavi, O. Squire, A. Pevsner, S.M. Larson, J.L. Humm, Quantitation of respiratory motion during 4D-PET/CT acquisition, Med Phys. 31 (2004) 1333–8. https://doi.org/10.1118/1.1739671.

[18] Y. Cui, J. Bowsher, J. Cai, F.-F. Yin, Impact of moving target on measurement accuracy in 3D and 4D PET imaging—a phantom study, Advances in Radiation Oncology. 2 (2017) 94–100. https://doi.org/10.1016/j.adro.2016.12.002.

[19] A. Protik, M. van Herk, M. Witte, J.-J. Sonke, The impact of breathing amplitude on dose homogeneity in intensity modulated proton therapy, Physics and Imaging in Radiation Oncology. 3 (2017) 11–16. https://doi.org/10.1016/j.phro.2017.07.004.

[20] M. Defrise, P.E. Kinahan, D.W. Townsend, C. Michel, M. Sibomana, D.F. Newport, Exact and approximate rebinning algorithms for 3-D PET data, IEEE Trans Med Imaging. 16 (1997) 145–58. https://doi.org/10.1109/42.563660.

[21] J.B. Thibault, K.D. Sauer, C.A. Bouman, J. Hsieh, A three-dimensional statistical approach to improved image quality for multislice helical CT, Med Phys. 34 (2007) 4526–44. https://doi.org/10.1118/1.2789499.

[22] L.H. Chen, C. Jin, J.Y. Li, G.L. Wang, Y.J. Jia, H.F. Duan, N. Pan, J. Guo, Image quality comparison of two adaptive statistical iterative reconstruction (ASiR, ASiR-V) algorithms and filtered back projection in routine liver CT, Br J Radiol. 91 (2018) 20170655. https://doi.org/10.1259/bjr.20170655.

[23] J. Nuyts, D. Beque, P. Dupont, L. Mortelmans, A concave prior penalizing relative differences for maximum-a-posteriori reconstruction in emission tomography, IEEE Transactions on Nuclear Science. 49 (2002) 56–60. https://doi.org/10.1109/tns.2002.998681.

[24] S. Ahn, S.G. Ross, E. Asma, J. Miao, X. Jin, L. Cheng, S.D. Wollenweber, R.M. Manjeshwar, Quantitative comparison of OSEM and penalized likelihood image reconstruction using relative difference penalties for clinical PET, Phys Med Biol. 60 (2015) 5733–51. https://doi.org/10.1088/0031-9155/60/15/5733.

[25] M.S. Tohme, J. Qi, Iterative image reconstruction for positron emission tomography based on a detector response function estimated from point source measurements, Phys Med Biol. 54 (2009) 3709–25. https://doi.org/10.1088/0031-9155/54/12/007.

[26] A. Rezaei, G. Schramm, K. Van Laere, J. Nuyts, Estimation of Crystal Timing Properties and Efficiencies for the Improvement of (Joint) Maximum-Likelihood Reconstructions in TOF-PET, IEEE Trans Med Imaging. 39 (2020) 952–963. https://doi.org/10.1109/TMI.2019.2938028.

[27] D. Brasse, P.E. Kinahan, C. Lartizien, C. Comtat, M. Casey, C. Michel, Correction methods for random coincidences in fully 3D whole-body PET: impact on data and image quality, J Nucl Med. 46 (2005) 859–67.

[28] H. Zaidi, M.L. Montandon, Scatter Compensation Techniques in PET, PET Clin. 2 (2007) 219–34. https://doi.org/10.1016/j.cpet.2007.10.003.

[29] L. Fin, P. Bailly, J. Daouk, M.-E. Meyer, Motion correction based on an appropriate system matrix for statistical reconstruction of respiratory-correlated PET acquisitions., Comput Methods Programs Biomed. 96 (2009) e1-9. https://doi.org/10.1016/j.cmpb.2009.05.001.

[30] P. Bailly, R. Bouzerar, T. Shields, M.E. Meyer, J. Daouk, Benefits of respiratory-gated 18F-FDG PET acquisition in lung disease, Nucl Med Commun. 39 (2018) 44–50. https://doi.org/10.1097/MNM.0000000000000772.

[31] J. Oddstig, S. Leide Svegborn, H. Almquist, U. Bitzén, S. Garpered, F. Hedeer, C. Hindorf, J. Jögi, L. Jönsson, D. Minarik, R. Petersson, A. Welinder, P. Wollmer, E. Trägårdh, Comparison of conventional and Si-photomultiplier-based PET systems for image quality and diagnostic performance, BMC Med Imaging. 19 (2019) 81. https://doi.org/10.1186/s12880-019-0377-6.

[32] V. Golovin, V. Saveliev, Novel type of avalanche photodetector with Geiger mode operation, Nuclear Instruments and Methods in Physics Research Section A:

Accelerators, Spectrometers, Detectors and Associated Equipment. 518 (2004) 560–564. https://doi.org/10.1016/j.nima.2003.11.085.

[33] H.M. Hudson, R.S. Larkin, Accelerated image reconstruction using ordered subsets of projection data, IEEE Trans Med Imaging. 13 (1994) 601–609. https://doi.org/10.1109/42.363108.

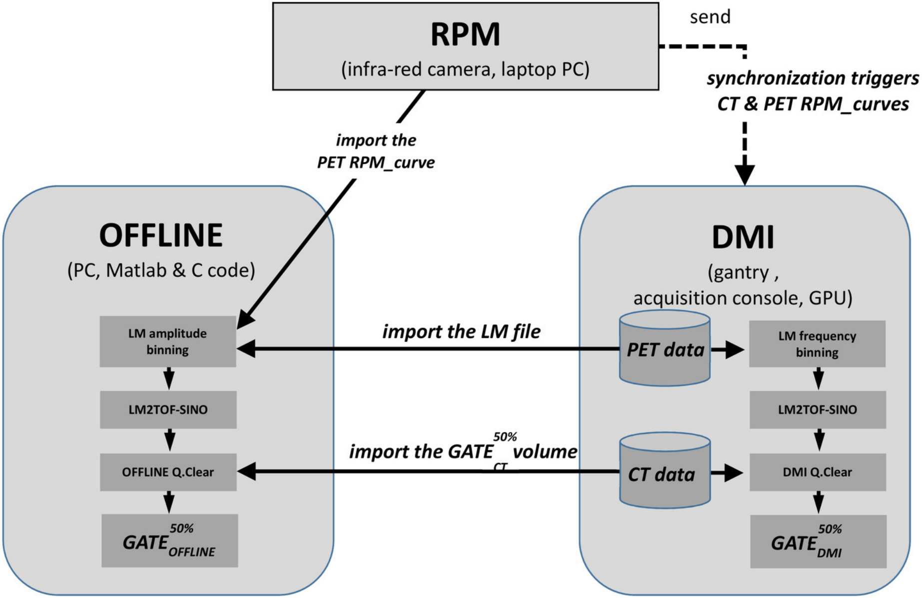
RPM
(infra-red camera, laptop PC)
send
synchronization triggers
CT & PET RPM_curves
import the
PET RPM_curve
OFFLINE
(PC, Matlab & C code)
LM amplitude binning
LM2TOF-SINO
OFFLINE Q.Clear
$GATE^{50\%}_{OFFLINE}$
import the LM file
import the $GATE^{50\%}_{CT}$ volume
DMI
(gantry ,
acquisition console, GPU)
PET data
CT data
LM frequency binning
LM2TOF-SINO
DMI Q.Clear
$GATE^{50\%}_{DMI}$

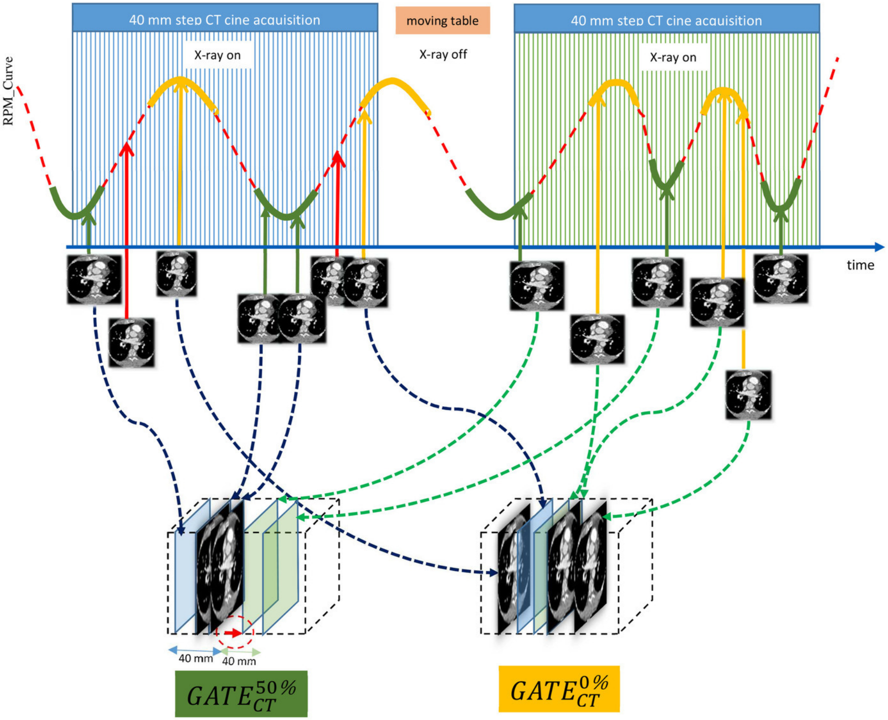
40 mm step CT cine acquisition
moving table
40 mm step CT cine acquisition
X-ray on
X-ray off
X-ray on
RPM_Curve
time
40 mm
40 mm
$GATE_{CT}^{50\%}$
$GATE_{CT}^{0\%}$

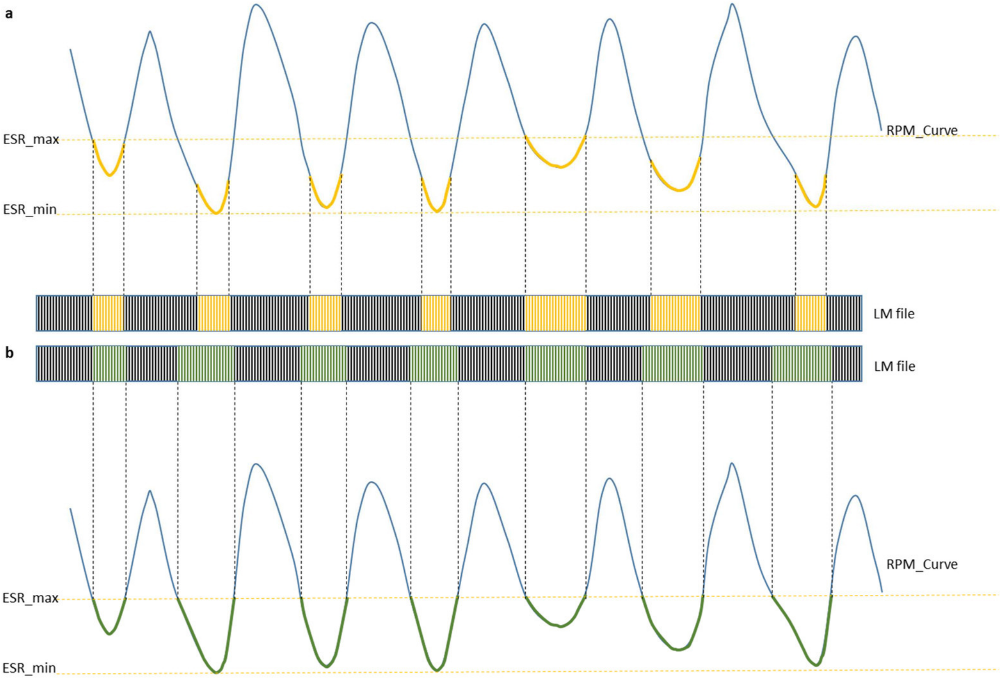
a
ESR_max
ESR_min
RPM_Curve
LM file
b
LM file
RPM_Curve
ESR_max
ESR_min

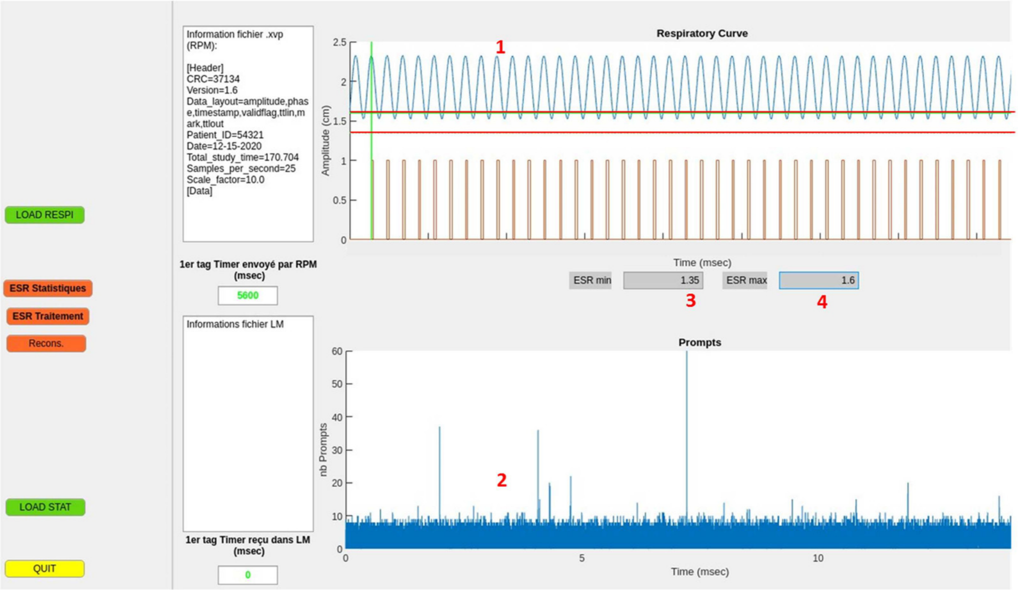

```
Information fichier .xvp
(RPM):

[Header]
CRC=37134
Version=1.6
Data_layout=amplitude,phas
e,timestamp,validflag,ttlin,m
ark,ttlout
Patient_ID=54321
Date=12-15-2020
Total_study_time=170.704
Samples_per_second=25
Scale_factor=10.0
[Data]
```

1er tag Timer envoyé par RPM (msec)

5600

ESR min 1.35

ESR max 1.6

Informations fichier LM

1er tag Timer reçu dans LM (msec)

0

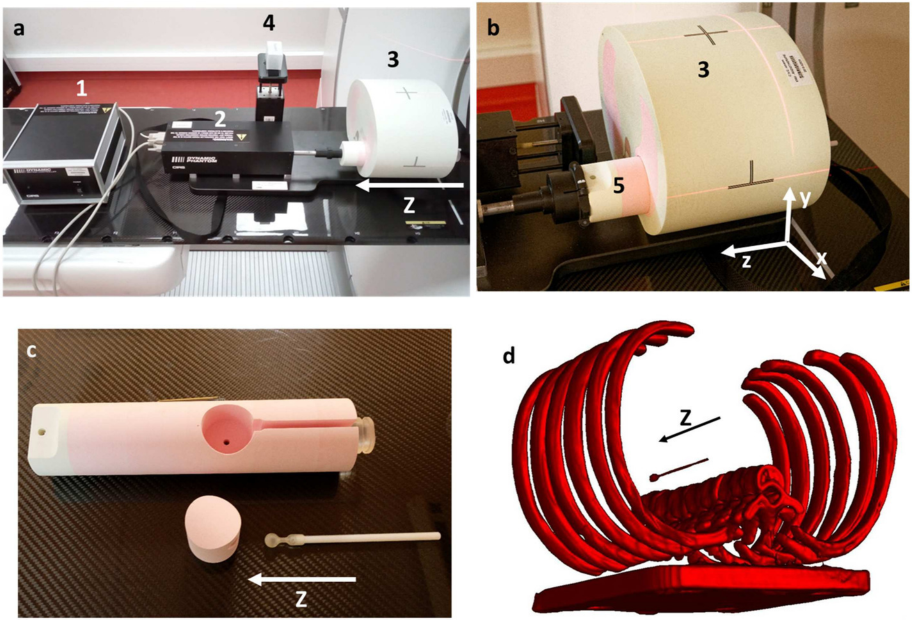
a
4
3
1
2
DYNAMIC PHANTOM
Z
b
3
5
y
z
x
c
Z
d
Z

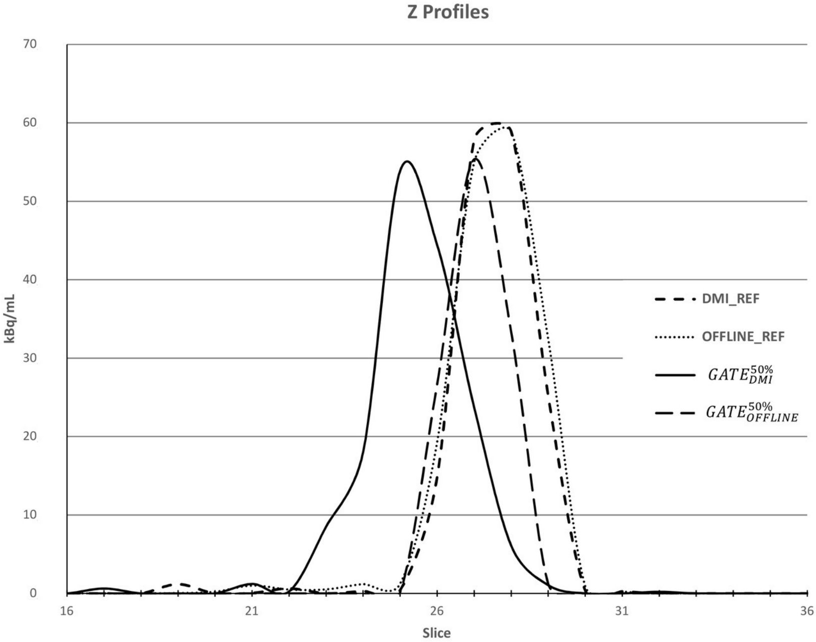
Z Profiles
70
60
50
40
30
20
10
0
kBq/mL
16
21
26
31
36
Slice
DMI_REF
OFFLINE_REF
$GATE_{DMI}^{50\%}$
$GATE_{OFFLINE}^{50\%}$

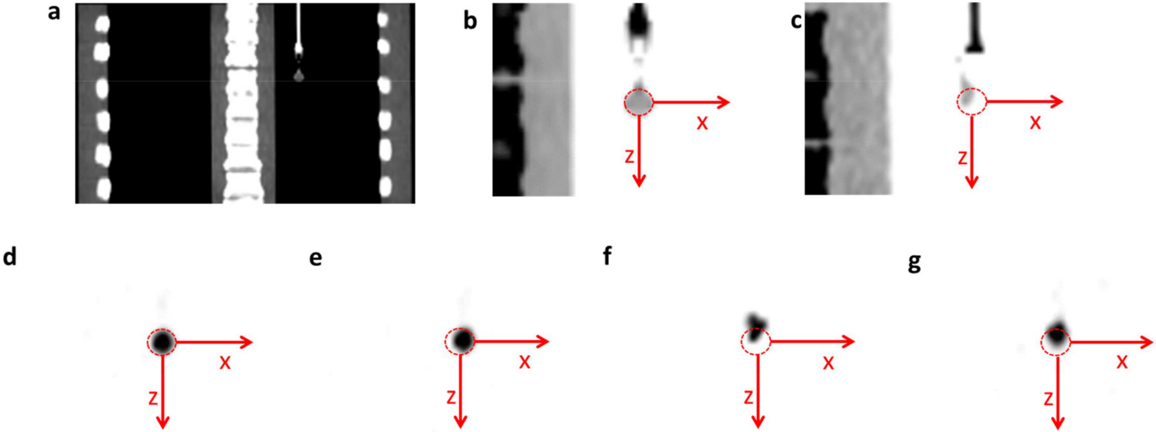
a
b
X
Z
c
X
Z
d
X
Z
e
X
Z
f
X
Z
g
X
Z

	DMI_REF	OFFLINE_REF	$GATE_{DMI}^{50\%}$	$GATE_{OFFLINE}^{50\%}$
maximum value (kBq/mL)	58.89	58.86	53.89	55.65
x (256 voxels)	145	143	146	143
y (256 voxels)	144	145	146	146
z (71 slices)	28	28	25	27
distance (mm)	NA	6.11	9.22	8.22
NMSE	NA	0.01	1.13	0.17
FWHM (mm)	7.07	7.14	7.64	7.3
FWTM (mm)	12.27	12.79	15.4	11.8

Abbreviations. NA: not applicable; NMSE: normalized mean square error; FWHM: full width at half-maximum; FWTM: full width at tenth-maximum